



Article

Synergistic Removal of Cr(VI) Utilizing Oxalated-Modified Zero-Valent Iron: Enhanced Electron Selectivity and Dynamic Fe(II) Regeneration

Song Hou ^{1,2}, Jiangkun Du ^{3,*} , Haibo Ling ^{1,2,3}, Sen Quan ^{1,2}, Jianguo Bao ³  and Chuan Yi ^{1,2,*}

¹ Hubei Provincial Academy of Eco-Environmental Sciences, Wuhan 430072, China; housong@hbaes.ac.cn (S.H.); linghaibo@hbaes.ac.cn (H.L.); quansen@hbaes.ac.cn (S.Q.)

² Hubei Key Laboratory of Pollution Damage Assessment and Environmental Health Risk Prevention and Control, Wuhan 430072, China

³ School of Environmental Studies, China University of Geosciences, Wuhan 430074, China; bjianguo@cug.edu.cn

* Correspondence: dujk@cug.edu.cn (J.D.); yichuan@hbaes.ac.cn (C.Y.)

Abstract: To address the challenges of environmental adaptability and passivation in nanoscale zero-valent iron (nFe⁰) systems, we developed oxalate-modified nFe⁰ (nFe_{oxa}) through a coordination-driven synthesis strategy, aiming to achieve high-efficiency Cr(VI) removal with improved stability and reusability. Structural characterization (STEM and FT-IR) confirmed the formation of a FeC₂O₄/nFe⁰ heterostructure, where oxalate coordinated with Fe(II) to construct a semiconductor interface that effectively inhibits anoxic passivation while enabling continuous electron supply, achieving 100% Cr(VI) removal efficiency within 20 min at an optimal oxalate/Fe molar ratio of 1/29. Mechanistic studies revealed that the oxalate ligand accelerates electron transfer from the Fe⁰ core to the surface via the FeC₂O₄-mediated pathway, as evidenced by EIS and LSV test analyses. This process dynamically regenerates surface Fe(II) active sites rather than relying on static-free Fe(II) adsorption. XPS and STEM further demonstrated that Cr(VI) was reduced to Cr(III) and uniformly co-precipitated with Fe(II/III)-oxalate complexes, effectively immobilizing chromium. The synergy between the protective semiconductor layer and the ligand-enhanced electron transfer endows nFe_{oxa} with superior reactivity. This work provides a ligand-engineering strategy to design robust nFe⁰-based materials for sustainable remediation of metal oxyanion-contaminated water.

Keywords: nano zero-valent iron; sodium oxalate; Cr(VI); reduction; electron transfer



Academic Editor: Luca Di Palma

Received: 27 March 2025

Revised: 18 April 2025

Accepted: 20 April 2025

Published: 28 April 2025

Citation: Hou, S.; Du, J.; Ling, H.; Quan, S.; Bao, J.; Yi, C. Synergistic Removal of Cr(VI) Utilizing Oxalated-Modified Zero-Valent Iron: Enhanced Electron Selectivity and Dynamic Fe(II) Regeneration. *Nanomaterials* **2025**, *15*, 669. <https://doi.org/10.3390/nano15090669>

Copyright: © 2025 by the authors. Licensee MDPI, Basel, Switzerland. This article is an open access article distributed under the terms and conditions of the Creative Commons Attribution (CC BY) license (<https://creativecommons.org/licenses/by/4.0/>).

1. Introduction

Chromate (Cr(VI)) contamination in water has long been seen as a critical issue globally. Chromium primarily exists in the form of Cr(III) and Cr(VI). Cr(III) has low toxicity and is recognized as a crucial trace element for mammals, while Cr(VI) possesses approximately 1000 times greater toxicity than the Cr(III) species [1]. Improper intake or long-term exposure of Cr(VI) can cause respiratory cancer, reproductive difficulties, and severe liver damage; thus, Cr(VI) has been recognized as a dangerous pollutant with the highest priority [2,3]. Therefore, efficient treatment of Cr(VI)-bearing wastewater has become as a vital task for sustainable industrial activities in the fields of electroplating, ore mining, metalworking, and leather manufacturing [4–6].

In the most recent decades, nanoscale zero-valent iron (nFe⁰) has been demonstrated to be an effective and eco-friendly material for in situ chemical remediation of Cr(VI)-

contaminated sites owing to its reductive capability [7,8]. However, the advantages of $n\text{Fe}^0$ are also accompanied by characteristics of unstable and easy aggregation, owing to strong surface energy of nanoparticles, the weaker van der Waals force action, and the magnetic properties of iron [9–11]. A typical phenomenon of this is that $n\text{Fe}^0$ is highly susceptible to air passivation with formation of a surface oxide film, which can hinder the electron transfer and substance diffusion in the solid–liquid interface, resulting in decreased adsorption capacity and reductive reactivity of $n\text{Fe}^0$ [12–14]. Consequently, it is of practical importance to improve the inter-particle dispersion and stability of $n\text{Fe}^0$ particles.

To enhance the reactivity against surface passivation, numerous studies have focused on the modification of $n\text{Fe}^0$ at the level of material surface or the entire body to augment interface electronic transfer [15,16]. There may be three ways for electrons to transfer from the iron core to the surface, where they react with heavy metal ions: (1) direct electron transfer through surface defects of $n\text{Fe}^0$ particles, (2) a semiconductor composed of Fe_2O_3 and FeOOH iron oxide for electron transfer, (3) Fe(II) on the surface of $n\text{Fe}^0$ serves as an electron donor [17]. Normally, the outer iron oxide shell of $n\text{Fe}^0$ is covered by hydrophilic hydroxyl groups due to the spontaneous hydrolysis of $n\text{Fe}^0$ [18], leading to a low electron utilization efficiency of $n\text{Fe}^0$.

To date, a variety of approaches have been intensively investigated to modify $n\text{Fe}^0$ for enhanced pollutant degradation and electron selectivity, such as bimetallic iron, surfactant modification, and sulfidation [19–21]. For instance, the formation of bimetallic nanomaterials (M^0/Fe^0) can avoid the wasteful oxidation of $n\text{Fe}^0$ with water [22,23], increase the catalytic production of reactive atomic hydrogen, and decrease the deposition of corrosion byproducts, thereby accelerating the reduction kinetics towards target pollutants [24]. Furthermore, attempts of surface surfactant coating, such as polyelectrolytes and biopolymers [25,26], can effectively control the nucleation and aggregation of $n\text{Fe}^0$ particles, therefore, increasing reactivity by enhancing the iron-contaminant interaction [27]. Arunkumar et al. [28] have verified that the modification with polyvinyl pyrrolidone (PVP) and carboxymethyl cellulose (CMC) can improve the steric hindrance, stability, dispersion and mobility of $n\text{Fe}^0$ particles. Moreover, the sulfidation of $n\text{Fe}^0$ using different vulcanizing agents (Na_2S , $\text{Na}_2\text{S}_2\text{O}_3$, and $\text{Na}_2\text{S}_2\text{O}_4$) has attracted particular interest in recent years. It was suggested that thiol groups would partly replace surface hydroxyl groups during $n\text{Fe}^0$ sulfidation in order to improve the electron selectivity and electron utilization efficiency of $n\text{Fe}^0$ for the removal of contaminants [29]. However, these existing modification methods also have some drawbacks in terms of cost, effectiveness and clean production. For instance, bimetallic nanoparticles are too expensive for large-scale application, while surfactant or sulfidated modification may result in secondary pollution of organics and H_2S , respectively, as well as high selectivity toward some specific pollutants [30–32]. On this account, the development of alternative $n\text{Fe}^0$ -based materials with an environmentally benign nature is highly desired and of great interest to actuate wider applications.

In addition to the aforementioned modifiers, low-molecular-weight organic acids (LMWOAs), including lactic, citric, malic and oxalic acids, have drawn particular attention in material modification in recent years. Typically, LMWOAs are widely available in natural environments [33,34]. They can be produced from plant root secretions, soil organic matter decomposition, and microbial metabolites, and are typically characterized by one or more carboxyl groups, with strong chelating capacity with multivalent metal cations [35,36]. Therefore, LMWOAs are expected to alter the surface charge of $n\text{Fe}^0$, thus reducing the tendency of particle agglomeration, or alleviating iron passivation through the formation of complex compounds [37,38]. Yuan et al. [39] demonstrated that S- $n\text{Fe}^0$ and LMWOAs exhibited significant synergistic promotion in the removal of Cr(VI) . Further studies showed that LMWOAs promoted various aspects of diffusion, adsorption and complexation of

Cr(VI) on the S-nFe⁰ surface, which, in turn, improves the electron selectivity for Cr(VI). Furthermore, tartrate or malate were reported to enhance the adsorption of Cr(VI) in the presence of S-nFe⁰ and accelerate the dissolution of the iron passivation layer through the formation of reactive nFe⁰-ligand systems either under anoxic or aerobic conditions [40,41]. In addition, compared to other LMWOAs, OA is non-toxic and harmless and can promote the dissolution of Fe(II) under acidic conditions, while C₂O₄^{2−} has a π -conjugated structure, and the delocalized electrons of C₂O₄^{2−} are favorable for the reduction of Fe(III) to Fe(II) [42–44]. Meanwhile, as a clean and effective remediation agent, oxalic acid is effective in improving pollutant degradation and removal efficiency. Wu et al. [45] found that the oxidized layer on the Fe⁰ surface was replaced by a ferrous oxalate shell layer through the ball milling process, accelerating the dissolution of Fe⁰ to generate Fe(II) for PS activation, which can significantly degrade pollutants. Li et al. [46] reported that the removal efficiency of Cr(VI) from wastewater can be effectively improved by using waste biomass N-doped lignocellulosic charcoal as a catalyst and OA as media. In addition, OA could also facilitate the corrosion of nFe⁰, accelerating the release of Fe(II). Since the redox potential of Cr(VI)/Cr(III) (1.33 V vs. NHE) is higher than that of Fe(III)/Fe(II) (0.77 V vs. NHE), a large amount of Fe(II) is produced, which significantly enhances the heterogeneous and homogeneous reduction of Cr(VI) in solution [39]. Therefore, the electron transfer pathway and the electron selectivity of Fe⁰ are also changed accordingly during the removal of Cr using OA-modified promoted Fe⁰. However, studies on the electron transfer capacity of oxalate-modified nFe⁰ have been very limited to date. Whether the primary pathway of electron transfer for Cr(VI) reduction by nFe⁰ is directly from nFe⁰ to Cr(VI) or from Fe(II) to Cr(VI) after the dissolution of nFe⁰, the process is currently unknown, which would be an obstacle to the application of nFe_{oxa} on the remediation of Cr(VI).

In order to address this gap, the objective of this research was to enhance the Cr(VI) removal property of nFe⁰, and the performance of nFe_{oxa} at different C₂O₄^{2−}/Fe molar ratios was tested from the perspective of reductive Cr(VI) removal. This study examined how different positive anions, oxygenated anion, humic acid, and the lifespan of nFe_{oxa} influence its ability to adapt to the aquatic ecosystem. Finally, the reaction mechanism in regard to the synergistic removal of Cr(VI) was unveiled using various tools, including fundamental electrochemical analysis and solid characterizations. This study presented a new insight into Cr(VI) removal, which was beneficial to understand the application boundaries of nFe_{oxa} for Cr(VI) remediation, and provided more theoretical guidance for the subsequent oxalic acid-modified materials.

2. Materials and Methods

2.1. Chemicals and Materials

Sodium borohydride (NaBH₄), sodium sulfide (Na₂S·9H₂O), iron sulfate (FeSO₄·7H₂O), sodium oxalate (Na₂C₂O₄), potassium bichromate (K₂Cr₂O₇), sulfuric acid (H₂SO₄), sodium hydroxide (NaOH), diphenyl carbamide (C₁₃H₁₄N₄O), humic acid (HA), sodium carbonate (Na₂CO₃), and ethanol were purchased from Sinopharm Chemical Reagent Co., Ltd. (Shanghai, China) at an analytical grade. The deoxygenated water was prepared by purging deionized water with pure nitrogen for 1 h prior to use.

2.2. Preparation of Oxalated nFe⁰

The oxalated nano-scale zero-valent iron particles (nFe_{oxa}) were prepared through the liquid phase reduction method. Briefly, ferrous sulfate, sodium oxalate and NaBH₄ were dissolved in deoxygenated water, respectively. Then, the NaBH₄ solution was mixed with the solution of sodium oxalate to obtain the NaBH₄/Na₂C₂O₄ mixture, which was added dropwise into the FeSO₄ solution in a three-necked flask equipped with mechanical

stirring under anaerobic conditions. After stirring for 20 min, FeSO_4 was fully reduced to zero-valent iron. The black particles generated in the three-neck flask were then isolated using a magnet, thoroughly washed three times with distilled water and ethanol, and ultimately dried in a vacuum oven at $60\text{ }^\circ\text{C}$ for 12 h. As expected, nFe_{oxa} particles with different $\text{C}_2\text{O}_4^{2-}/\text{Fe}^{2+}$ molar ratios, namely 1/14, 1/19, 1/29 and 1/58, were obtained and flagged as $\text{nFe}_{\text{oxa}}(\text{x}/\text{y})$, where x and y refer to the molarity of $\text{C}_2\text{O}_4^{2-}$ and Fe^{2+} , respectively. For instance, $\text{nFe}_{\text{oxa}}(1/29)$ denotes oxalated $\text{nFe}(0)$ with a $\text{C}_2\text{O}_4^{2-}/\text{Fe}^{2+}$ molar ratio of 1/29.

2.3. Batch Experiments of Cr(VI) Removal

The batch experiments of Cr(VI) removal were carried out in a 250 mL beaker containing 100 mL of the 10 mg/L Cr(VI) solution. The initial solution pH was adjusted with diluted HCl and NaOH. To initiate the reaction, 0.1 g of nFe_{oxa} particles was injected into the beaker, and the reaction solution was thoroughly mixed by mechanical stirring (300 rpm) at ambient conditions. At specified time intervals, a 1 mL sample was taken and subsequently filtered using a $0.22\text{ }\mu\text{m}$ polyethersulfone filter before analysis.

This study examined how the $\text{C}_2\text{O}_4^{2-}/\text{Fe}^{2+}$ molar ratio (1/14, 1/19, 1/29 and 1/58), the dosage of the material (ranging from 0.3 to 1.5 g/L), the presence of co-existing anions and humic acid (ranging from 10 to 80 mg/L), as well as the initial concentration of Cr(VI) (10–50 mg/L) affected the removal of Cr(VI). In addition, the stability property of nFe_{oxa} after the reaction was further evaluated. Typically, the used nFe_{oxa} particles were separated from the reacted solutions with the help of the magnet and washed with deoxygenated DI water, and then the fresh Cr(VI) solution was added to react with the used Fe_{oxa} particles once again.

2.4. Analysis

Characterization of the nFe_{oxa} particles, both prior to and following their reaction with Cr(VI), was performed using Transmission Electron Microscopy (TEM, CM12/STEM, Philips, Amsterdam, The Netherlands) equipped with an energy-dispersive spectrometer (EDS, Themis Z, Thermo Fisher Scientific, Waltham, MA, USA), X-ray Diffraction (XRD, X'Pert Pro, PANalytical, Malvern, UK), Scanning Transmission Electron Microscopy (STEM, Quanta 450, Thermo Fisher Scientific, Waltham, MA, USA) with high-angle annular dark-field imaging and phase-mapping capabilities, Brunauer–Emmett–Teller (BET) surface analysis (ASAP 2020, Micromeritics, Norcross, GA, USA), Fourier-Transform Infrared Spectroscopy (FT-IR, Nicolet iS50 ABX, Thermo Fisher Scientific, Waltham, MA, USA), X-ray Photoelectron Spectroscopy (XPS, VG Multilab 2000, VG Scientific, Edgewood, MD, USA) and various electrochemical tests. A three-electrode system was utilized for electrochemical analyses, operating within a voltage range of -2.0 V to 2.0 V at a scanning of 0.05 V s^{-1} employing a VersaSTAT 3. The working electrode consisted of a stainless-steel mesh coated with particles (1 cm^2), while Ag/AgCl and Pt wire served as the reference and counter electrodes, respectively. For all electrochemical experiments, $0.1\text{ M Na}_2\text{SO}_4$ acted as the electrolyte. The concentrations of Cr(VI) in the aqueous solution were quantified through the 1,5-diphenylcarbazide colorimetric method, measured at 540 nm using a UV–visible spectrophotometer (UV/Vis, UV5500PC, Shanghai Yuanxi Instrument Co., Ltd., Shanghai, China), demonstrating a detection limit of 0.004 mg/L and a linear range up to 1.0 mg/L . Additionally, the aqueous concentration of Fe(II) was determined via the 1,10-phenanthroline colorimetric method at a wavelength of 510 nm on the same spectrophotometer.

3. Results and Discussion

3.1. Characterization of $n\text{Fe}_{\text{oxa}}$

The pristine $n\text{Fe}_{\text{oxa}}$'s morphology and microstructure were analyzed using TEM and STEM imaging (Figure 1a,b), along with phase mapping. The fresh $n\text{Fe}_{\text{oxa}}$ exhibited a characteristic chain structure [47]. From the TEM and STEM images, typical chain-like formations were retained in the fresh $n\text{Fe}_{\text{oxa}}$, while spherical and rectangular shapes were observed due to aggregation and compression. When $n\text{Fe}^0$ was modified with oxalic acid, $n\text{Fe}_{\text{oxa}}$ was surrounded by a muslin-like lamellar structure, which would be the oxalate–iron complexes.

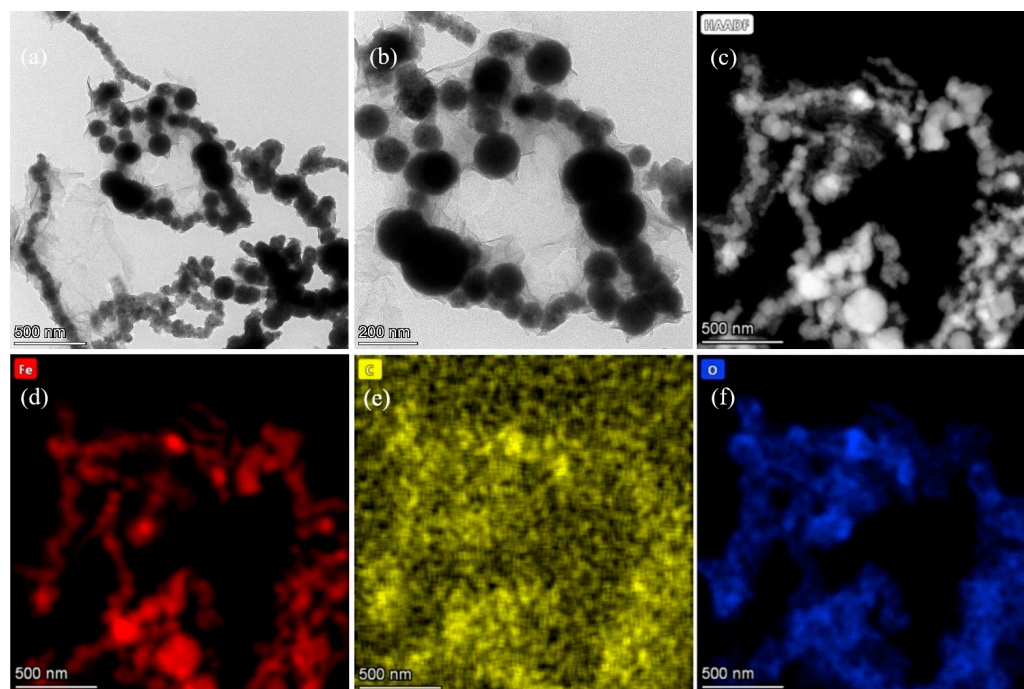


Figure 1. (a,b) TEM analysis of fresh $n\text{Fe}_{\text{oxa}}$ (S/Fe molar ratio = 1/29), (c) STEM image, (c–f) HAADF-STEM mappings of fresh $n\text{Fe}_{\text{oxa}}$ (1/29) (elements Fe, C, and O are denoted in red, yellow, and blue).

The STEM element map of $n\text{Fe}_{\text{oxa}}$ (Figure 1c,f) indicates that Fe species highly overlapped with the O element, whereas the C element is highly dispersed. Noteworthy, the signal of the C element enhanced in sites overlapped with the Fe element, indicating the coordination and complexation of oxalic acid with Fe(II). This is similar to the distribution law of the “tissue” observed in the TEM image, and it illustrates the success of the doping of sodium oxalate and the formation of oxalate–iron complexes.

To further delve into the effect of oxalic acid doping in $n\text{Fe}_{\text{oxa}}$, the mineral composition and crystallinity of $n\text{Fe}^0$ and $n\text{Fe}_{\text{oxa}}$ were compared by XRD characterization. As depicted in Figure 2, $n\text{Fe}^0$ both before and after oxalic acid modification exhibits a typical zero-valent iron diffraction peak at 44.6° . Weak characteristic diffraction peaks of Fe_3O_4 can be seen in the XRD spectrum of bare $n\text{Fe}^0$, signifying the presence of a thin Fe_3O_4 oxide layer on the surface of $n\text{Fe}^0$. However, there is no corresponding magnetite diffraction peak in the oxalic-acid-modified $n\text{Fe}_{\text{oxa}}$ material, indicating that the doping of oxalic acid can avoid the oxide layer formation on the surface of $n\text{Fe}^0$, thereby postponing the passivation process. Moreover, in conjunction with the outcomes of TEM and STEM, the passivation process was further constrained simultaneously by the existence of the oxalate–iron complexes. Here, the doping of oxalate acid can not only preserve the Fe(II) active sites of $n\text{Fe}_{\text{oxa}}$, but also increase the potential for the contact of pollutants with $n\text{Fe}_{\text{oxa}}$.

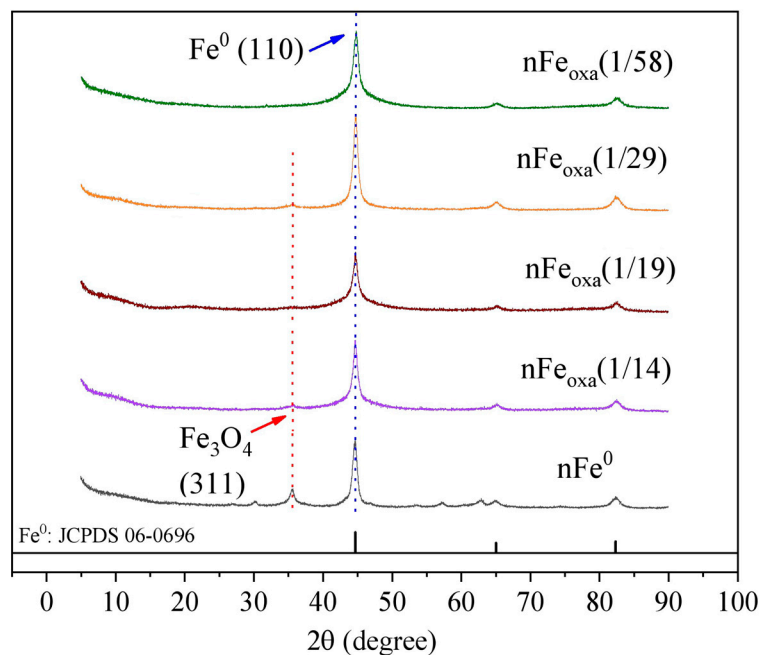


Figure 2. X-ray diffraction patterns of $n\text{Fe}^0$ and $n\text{Fe}_{\text{Oxa}}$ particles.

The N_2 sorption and desorption properties of $n\text{Fe}^0$ before and after oxalation were characterized, both of which showed type IV isotherm with an H3 hysteresis loop, as depicted in Figure 3, indicating a typical monolayer adsorption. Regardless of oxalation or not, most of the pores of $n\text{Fe}^0$ had diameters of 0–10 nm, ascribed to mesoporous particles. The BET surface areas of the $n\text{Fe}_{\text{Oxa}}(1/29)$ and $n\text{Fe}^0$ materials were determined to be $23.52 \text{ m}^2/\text{g}$ and $80.63 \text{ m}^2/\text{g}$, respectively, while their material pore volumes were $0.090041 \text{ cm}^3/\text{g}$ and $0.313722 \text{ cm}^3/\text{g}$ (Table 1). These results indicated that bare $n\text{Fe}^0$ without oxalate modification possessed a significantly larger specific surface area and pore volume than its oxalated counterpart. In contrast to the assumption that a smaller specific surface area would be commonly accompanied by less chemical adsorption and reductive sites on the material surface would also be reduced, the reactivity of $n\text{Fe}_{\text{Oxa}}$ herein was not attributed to a larger surface area but caused by a potential synergistic effect within the composite.

By comparing the particle size of the $n\text{Fe}_{\text{Oxa}}$ and $n\text{Fe}^0$ materials (Figure 4), the particle size of unmodified $n\text{Fe}^0$ particles is primarily concentrated around 3000 nm, while the particle sizes of $n\text{Fe}_{\text{Oxa}}$ modified with oxalic acid become smaller and decrease with the reduction in the oxalic $\text{C}_2\text{O}_4^{2-}/\text{Fe}^{2+}$ molar ratio. As presented in Table 2, the average particle size of $n\text{Fe}^0$ in this experiment is about 4–5 times that of the average particle size of the modified $n\text{Fe}_{\text{Oxa}}$ composites. The smaller particle size is beneficial to the migration and diffusion in water, and the stronger Brownian motion is beneficial for contact with free Cr(VI) and to expedite the removal of Cr(VI) . From the characterization results above, it can be observed that oxalic acid doping has a significant impact on the morphology, crystal form, specific surface area and particle size of $n\text{Fe}^0$, leading to a discrepancy between the physicochemical properties and reactivity of $n\text{Fe}_{\text{Oxa}}$ and $n\text{Fe}^0$. Consequently, it was essential to further elucidate the occurrence form of oxalic acid in $n\text{Fe}^0$.

Table 1. BET specific surface area and pore volume parameters of $n\text{Fe}^0$ and $n\text{Fe}_{\text{Oxa}}$ particles.

Materials	BET Surface Area (m^2/g)	Pore Diameter (nm)	Pore Volume (cm^3/g)
$n\text{Fe}^0$	80.6138	15.9322	0.313722
$n\text{Fe}_{\text{Oxa}}(1/29)$	23.5177	15.7567	0.090041

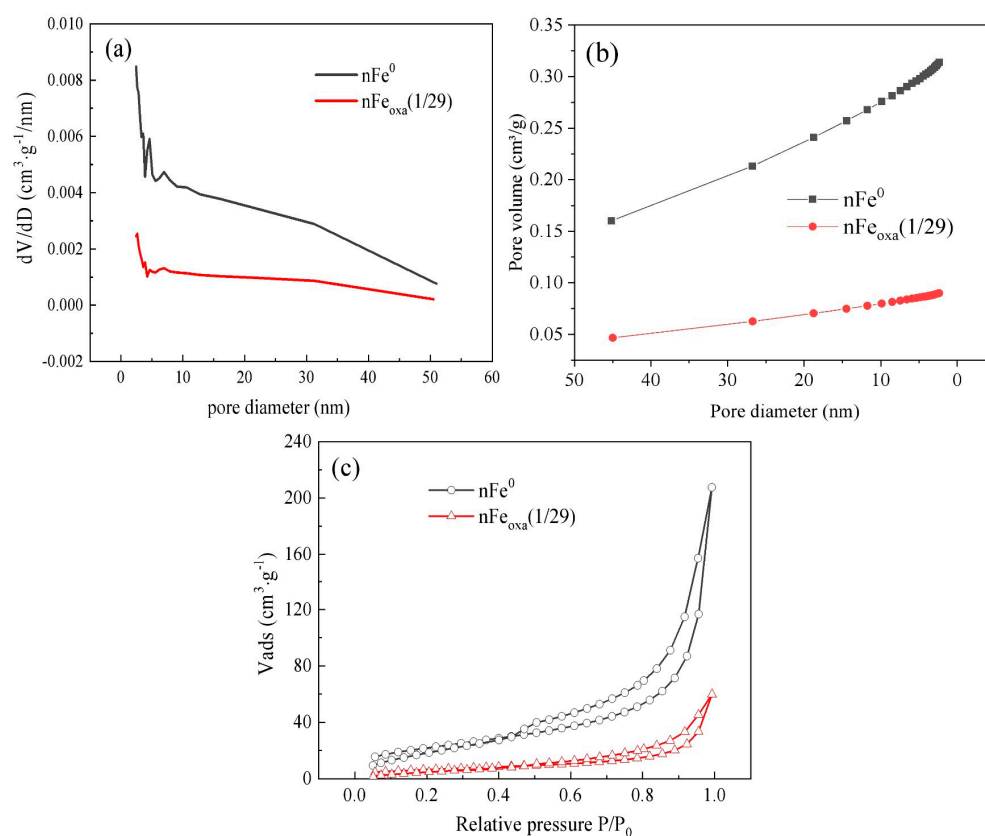


Figure 3. (a) Particle pore size distribution map; (b) cumulative pore volume map; (c) N_2 adsorption and desorption isotherms of $n\text{Fe}^0$ and $n\text{Fe}_{\text{oxa}}$.

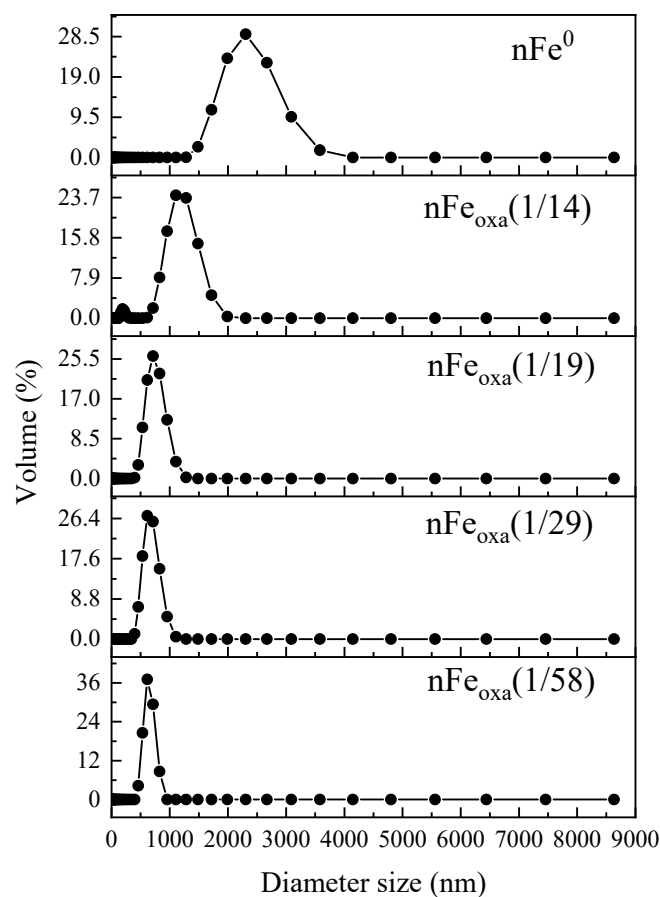
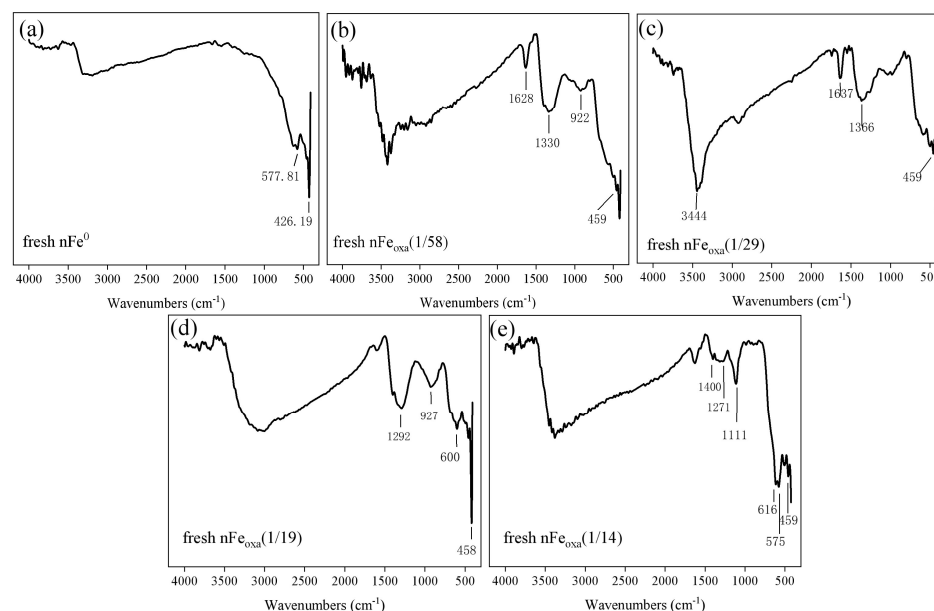


Figure 4. Particle size distribution of $n\text{Fe}^0$ and $n\text{Fe}_{\text{oxa}}$.

Table 2. Average particle size of $n\text{Fe}^0$ and $n\text{Fe}_{\text{oxa}}$ particles.

Materials	Particle Size D(50) (nm)
$n\text{Fe}^0$	2190
$n\text{Fe}_{\text{oxa}}$ (1/14)	641
$n\text{Fe}_{\text{oxa}}$ (1/19)	478
$n\text{Fe}_{\text{oxa}}$ (1/29)	483
$n\text{Fe}_{\text{oxa}}$ (1/58)	456

The FT-IR results of $n\text{Fe}_{\text{oxa}}$ and Fe^0 are presented in Figure 5. Compared to single $n\text{Fe}^0$, the newly emerged FT-IR spectra of $1620\text{--}1640\text{ cm}^{-1}$, $1270\text{--}1360\text{ cm}^{-1}$ and 1111 cm^{-1} can be recognized as consistent with the FT-IR vibration peaks of iron–oxalic acid complexes as reported previously [48]. The peak at wavenumber of 577 cm^{-1} and 927 cm^{-1} suggests the existence of magnetite and goethite on the material surface. This is consistent with the results of STEM and XRD, demonstrating the appearance of FeC_2O_4 and its coexistence with $\text{Fe}(0)$ during $n\text{Fe}_{\text{oxa}}$ formation.

**Figure 5.** FT-IR spectra of (a) $n\text{Fe}^0$, (b) $n\text{Fe}_{\text{oxa}}$ (1/58), (c) $n\text{Fe}_{\text{oxa}}$ (1/29), (d) $n\text{Fe}_{\text{oxa}}$ (1/19), and (e) $n\text{Fe}_{\text{oxa}}$ (1/14) of fresh $n\text{Fe}^0$ and $n\text{Fe}_{\text{oxa}}$ materials.

3.2. Effect of Different S/Fe Molar Ratios

As illustrated in Figure 6a, the $n\text{Fe}_{\text{oxa}}$ composite with varying $\text{Fe}^{2+}/\text{C}_2\text{O}_4^{2-}$ molar ratios demonstrated significantly higher Cr(VI) removal rates compared to pristine $n\text{Fe}^0$. Due to strong coordination and chelation ability [43], $\text{C}_2\text{O}_4^{2-}$ possessing two carboxyl groups could coordinate with iron atoms on the surface of iron oxides to form diverse iron oxide composite products [49–51]. Additionally, $\text{C}_2\text{O}_4^{2-}$ with conjugated π bond would be advantageous for the surface Fe(III) to obtain electrons from the iron core and then convert to Fe(II) [52]. The rapid electron transfer among Fe(0), Fe(III) and Fe(II) in the reaction interface is beneficial for the adsorption and reduction of Cr(VI), as well as the co-precipitation of Cr(III) with Fe(III) on the particle surface. When the molar ratio of $\text{C}_2\text{O}_4^{2-}/\text{Fe}^{2+}$ was 1/29, the prepared $n\text{Fe}_{\text{oxa}}$ (1/29) achieved the highest reactivity and completely removed Cr(VI) within 20 min. However, under the same conditions, the removal efficiency of Cr(VI) by $n\text{Fe}^0$ was only 68.5% in 20 min, and 88.7% after 1 h reaction. Furthermore, the results of the pseudo-second-order kinetic constants (Figure 6b) showed that the reactivity of $n\text{Fe}_{\text{oxa}}$ was not linearly related to the doping amount of oxalic acid.

The removal rate of Cr(VI) initially increased and then decreased with the increase in oxalic acid, and ultimately remained stable [53,54]. This result may be due to the fact that $\text{C}_2\text{O}_4^{2-}$ was negatively charged and showed a charge repulsion effect with Cr(VI). The oxalic acid was more likely to enhance the reduction activity and electron transfer rate of nFe^0 , and the change brought about by the oxalic acid doping also exists in an optimal balance. Therefore, in this study of the surface modification of micron zero-valent iron with oxalic acid, $\text{C}_2\text{O}_4^{2-}$ dissolves in the liquid phase [48]. When the doping ratio of oxalic acid is too high, a large amount of free oxalate ions in the reaction solution may cause the nanoparticles to dissociate, resulting in a decrease in the adsorption capacity of Cr(VI).

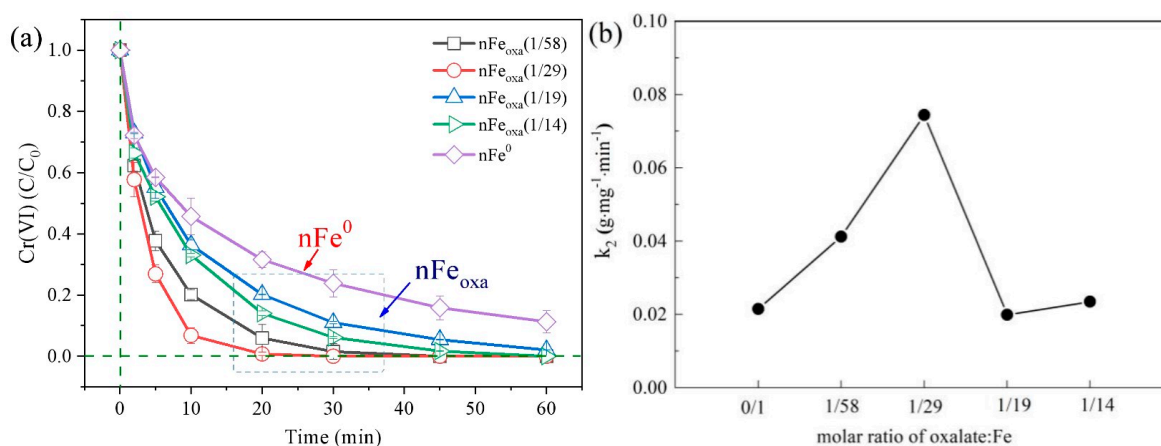


Figure 6. (a) Cr(VI) removal effect of nFe_{oxa} with different doping ratios of oxalic acid; (b) second-order kinetic constant change diagram.

3.3. Effect of Co-Existing Ions and Humic Acid

To investigate the impacts of co-existing water anions (such as PO_4^{3-} , CO_3^{2-} , NO_3^- , and Cl^-) and humic acid (HA) on Cr(VI) removal by nFe_{oxa} , both high and low concentrations were studied. According to previous reports, the co-existing ions in water can form surface metal complexes with the iron oxide layer on the surface of nFe^0 , which would promote the dissolution of the shell and enhance electron transfer [55–57]. Specifically, PO_4^{3-} and CO_3^{2-} can chelate, precipitate and passivate the ferrous irons, while NO_3^- can be reduced by nFe^0 [58]. Cl^- can promote the corrosion process of zero-valent iron, thereby accelerating the passivation of zero-valent iron [59,60].

As illustrated in Figure 7, Ca^{2+} and Mg^{2+} showed an insignificant effect on the removal of Cr(VI), where Cr(VI) can be completely removed. Previous studies demonstrated that the removal of pollutants in the system by metal cations is affected by the radius of their hydrated ions [61]. The radius sizes of Ca^{2+} , Mg^{2+} , and Cr^{6+} are 99 pm, 72 pm and 52 pm, respectively. Accordingly, a smaller ionic radius and higher charge would correspond to a greater degree of ion polarization and adsorption affinity [62]. At the same time, the addition of CaCl_2 and MgCl_2 introduces a significant amount of Cl^- , thus promoting nFe_{oxa} corrosion and enhancing aqueous conductivity, as well as expediting the electron transfer between nFe_{oxa} and Cr(VI) to facilitate the Cr(VI) removal [59].

Nevertheless, PO_4^{3-} , CO_3^{2-} and NO_3^- all restrained the removal of Cr(VI) in the system. PO_4^{3-} and CO_3^{2-} were expected to compete with Cr(VI) for active sites on the surface of nFe_{oxa} and simultaneously form complexes and co-precipitates with iron oxides on the particle surface. For instance, PO_4^{3-} can form Fe-PO_4^{3-} minerals with Fe(II), while CO_3^{2-} would be adsorbed onto the surface of nanoparticles, co-precipitate with Fe(II) as FeCO_3 , and occupy and deplete Fe(II) active sites, resulting in a reduction in the removal efficiency of Cr(VI) [63–65].

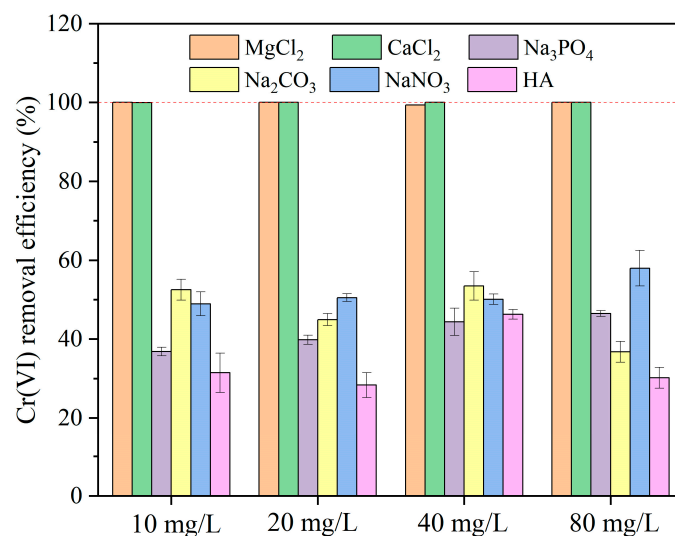


Figure 7. Effect of water anions and humic acid on Cr(VI) removal by nFe_{oxa} (reaction conditions: [nFe_{oxa}] = 1.0 g/L (C₂O₄^{2−}/Fe²⁺ molar ratio = 1/29), [Cr(VI)] = 10 mg/L, initial pH = 6, T = 25 °C).

Additionally, NO₃[−] inhibited the reduction of Cr(VI) by competing for electrons. Since the standard electrode potential of NO₃[−]/NO₂[−] (0.01 V) is higher than that of Fe²⁺/Fe (−0.44 V), NO₃[−] can compete with CrO₄^{2−} for Fe(II) and Fe(0) to be reduced to NO₂[−] [66–68]. Moreover, humic acid showed a remarkable inhibition to Cr(VI) removal by nFe_{oxa} (Figure 7). As viscous macromolecular organic matters in solution, humic acid can form complexes with surface iron species via abundant carboxyl functional groups, thus occupying nFe_{oxa} surface sites and impeding the interaction with Cr(VI) [69].

3.4. Reusability

Figure 8 presents the effect of five reuse times on Cr(VI) removal by nFe_{oxa}. The removal efficiency of Cr(VI) by nFe_{oxa} gradually decreased along the reuse times, which was nearly 50% after five times of reuse. According to previous reports, the removal rate of Cr(VI) dropped to 33.4% for the FeS-modified nFe⁰ material after three cycles, while the removal efficiency of Cr(VI) for nFe⁰ alone was 19.8% after three reuse runs. This finding indicated that nFe_{oxa} possessed good reusability in removing Cr(VI) [70].

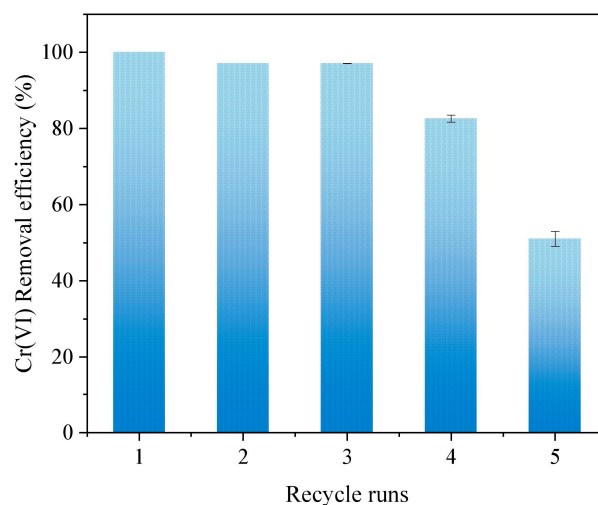


Figure 8. Reuse effect of nFe_{oxa} material in the Cr(VI) removal process.

Quenching Fe(II), recognized as a primary reductant and precipitator for Cr(VI), significantly influenced the sequestration of Cr(VI). As indicated in Figure 9a, the removal

efficiencies for both $n\text{Fe}^0$ and $n\text{Fe}_{\text{oxa}}$ saw a considerable reduction compared to the reaction that excluded 1,10-phenanthroline. After adding 1,10-phenanthroline for 60 min, the removal efficiency of Cr(VI) by $n\text{Fe}^0$ and $n\text{Fe}_{\text{oxa}}$ decreased by approximately 40% and 70%, respectively. It was obvious that Fe(II) played an essential role in the removal of Cr(VI) from the aqueous solution, and the contribution of Fe(II) to the removal of Cr(VI) was higher in $n\text{Fe}_{\text{oxa}}$ than in $n\text{Fe}^0$. In other words, the $n\text{Fe}_{\text{oxa}}$ surface produced significantly more Fe(II) active sites than $n\text{Fe}^0$ during the reaction. Further analyzing the change in Fe(II) concentration in Figure 9b, under the same reaction conditions with 1,10-phenanthroline present, the behavior of aqueous Fe(II) diverged. The Fe(II) concentration of $n\text{Fe}^0$ continued to increase with the reaction, while the Fe(II) concentration of $n\text{Fe}_{\text{oxa}}$ increased slowly and then remained stable after adding 1,10-phenanthroline. After 60 min of reaction, the concentration of Fe(II) in $n\text{Fe}^0$ was significantly higher than that in $n\text{Fe}_{\text{oxa}}$, indicating that $n\text{Fe}^0$ could produce more free Fe(II) for Cr(VI) reduction. However, $n\text{Fe}_{\text{oxa}}$ was based on the Fe(II) reactive component on the material surface for Cr(VI) reduction.

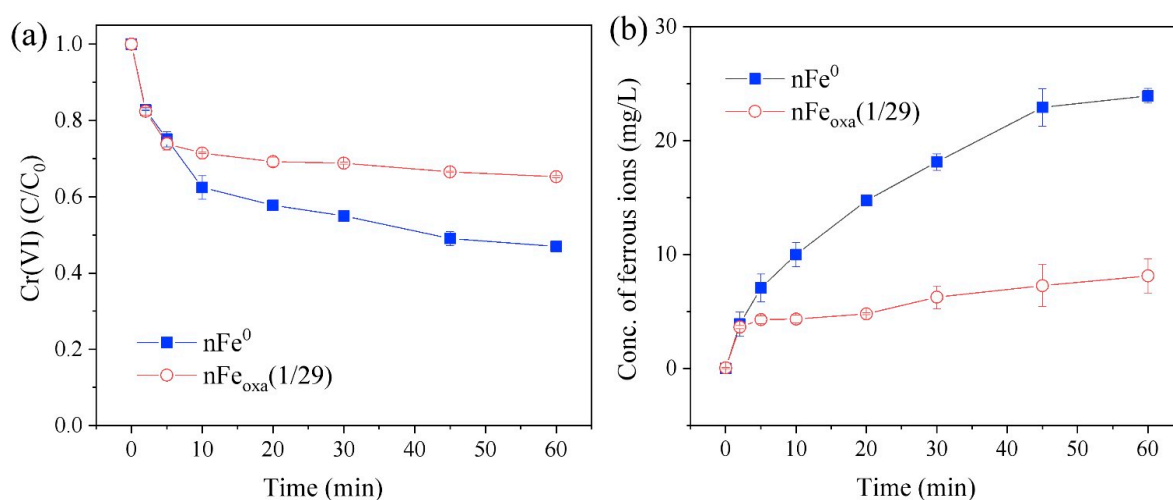


Figure 9. (a) The effect of 1,10-phenanthroline on the removal of Cr(VI) by $n\text{Fe}_{\text{oxa}}$ and $n\text{Fe}^0$, (b) release of Fe(II) with $n\text{Fe}_{\text{oxa}}$ and $n\text{Fe}^0$ of different S/Fe molar ratios in the presence of 1,10-phenanthroline.

Based on previous results of the BET test, it is indicated that the specific surface area of $n\text{Fe}_{\text{oxa}}$ was smaller than that of $n\text{Fe}^0$. Thus, the enhanced reactivity of $n\text{Fe}_{\text{oxa}}$, relative to $n\text{Fe}^0$, is unlikely to be ascribed to an increase in surface active sites but may stem from a more rapid rate of electron transfer during the reaction. To explore the charge transfer characteristics of $n\text{Fe}^0$ and $n\text{Fe}_{\text{oxa}}$, electrochemical impedance studies (EISs) were conducted. As shown in Figure 10a, the larger curve indicated that the electrode exhibited lower charge transfer capability and higher resistance, while $n\text{Fe}_{\text{oxa}}$ generated a much smaller curve than $n\text{Fe}^0$, suggesting that the electron transfer resistance of $n\text{Fe}_{\text{oxa}}$ was lower than that of bare $n\text{Fe}^0$. The reason for this phenomenon may be that the formation of an iron oxide passivation layer is avoided during the $\text{H}_2\text{C}_2\text{O}_4$ modification process, and the newly generated $\text{FeC}_2\text{O}_4/\text{Fe}^0$ semiconductor structure is beneficial for the transfer of charges.

Furthermore, through the linear sweep voltammetry (LSV) test of the material (Figure 10b), two oxidation peaks (0.75–1.43 V and 1.43–2.0 V) can be found in the LSV spectra of $n\text{Fe}_{\text{oxa}}$ and $n\text{Fe}^0$, which were ascribed to be the oxidation peak of $\text{Fe}(0) \rightarrow \text{Fe(II)}$ and $\text{Fe(II)} \rightarrow \text{Fe(III)}$. When the potential corresponding to the oxidation peak of the material was smaller, the reaction proceeded more easily. Correspondingly, the potential of $n\text{Fe}_{\text{oxa}}$ in the oxidation peak of $\text{Fe}(0) \rightarrow \text{Fe(II)}$ is similar to that of $n\text{Fe}^0$, while the potential of $n\text{Fe}_{\text{oxa}}$ in the oxidation peak of $\text{Fe(II)} \rightarrow \text{Fe(III)}$ is slightly smaller than that of $n\text{Fe}^0$, indicating that Fe(II) in $n\text{Fe}_{\text{oxa}}$ more easily acts as an electron donor to transfer electrons to Cr(VI).

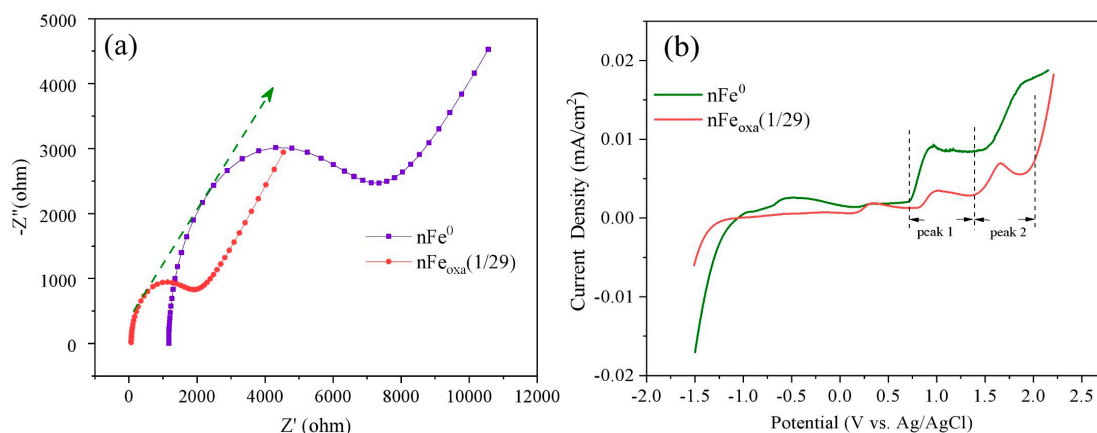


Figure 10. (a) EIS of $n\text{Fe}_{\text{Oxa}}$ and $n\text{Fe}^0$, (b) CV of $n\text{Fe}_{\text{Oxa}}$ and $n\text{Fe}^0$.

3.5. Mechanism of Cr(VI) Sequestration by $n\text{Fe}_{\text{Oxa}}$

The characteristics of $n\text{Fe}_{\text{Oxa}}$ following reactions were analyzed through the TEM, STEM and XPS techniques to gain a clearer insight into the reaction mechanism. The TEM image (Figure 11a,b) indicated that the surface morphology of the Cr-treated $n\text{Fe}_{\text{Oxa}}$ had changed considerably compared with that of the fresh $n\text{Fe}_{\text{Oxa}}$. The fresh $n\text{Fe}_{\text{Oxa}}$ material had an obvious spherical shape and smooth surface, while the Cr-treated $n\text{Fe}_{\text{Oxa}}$ had a significant tendency to agglomerate, with the boundary gradually blurring and the surface passivation layer apparently thickening. Numerous smaller particles formed on the surface of $n\text{Fe}_{\text{Oxa}}$, presumably caused by the formation of Fe-Cr strong oxides attached to the surface of the material after the reduction of Cr(VI). Meanwhile, in conjunction with the STEM elemental mapping of the reacted $n\text{Fe}_{\text{Oxa}}$ material (Figure 11c–f), it can be clearly observed that the Cr element was highly overlapped with the Fe and O elements, indicating that Cr was enriched on the $n\text{Fe}_{\text{Oxa}}$ surface.

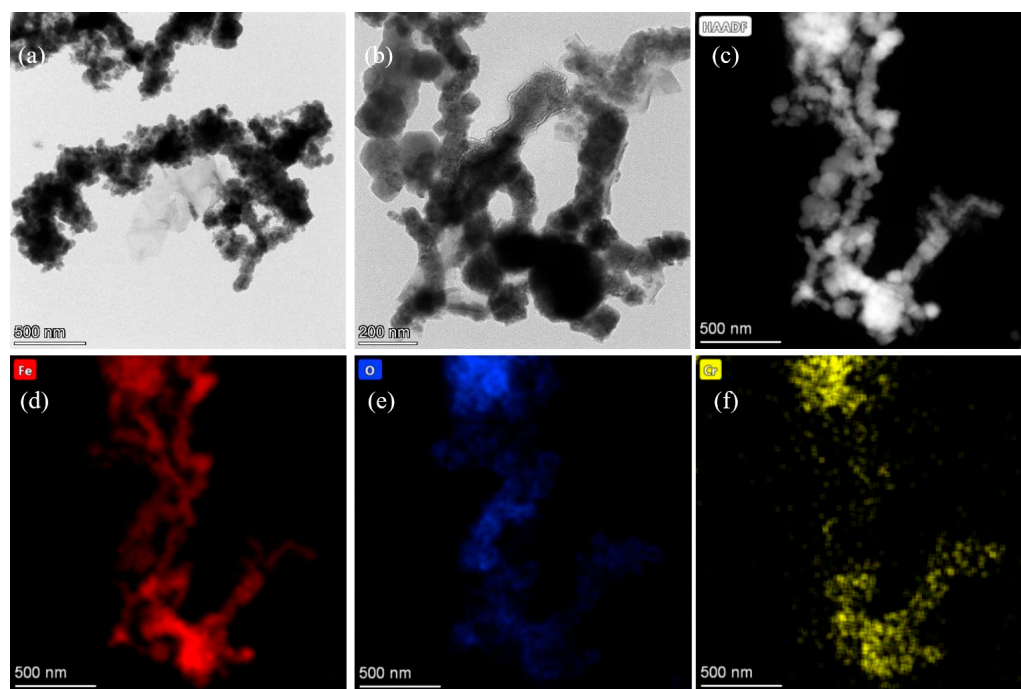


Figure 11. (a,b) The TEM results of Cr-treated $n\text{Fe}_{\text{Oxa}}(1/29)$, (c) STEM image, (c–f) HAADF-STEM mappings of Cr-treated $n\text{Fe}_{\text{Oxa}}(1/29)$ (elements Fe, O and Cr are denoted in red, blue and yellow).

Further investigation into the speciation of carbon (C), iron (Fe), oxygen (O), and chromium (Cr) in $n\text{Fe}_{\text{oxa}}$ prior to and post-reaction was conducted utilizing XPS. It can be seen from Figure 12a that the C 1s at 284.86 eV can be ascribed to the characteristic peak of the carboxyl group $\text{O}=\text{C}-\text{O}$ in the molecular structure of oxalic acid. The C content in $\text{O}=\text{C}-\text{O}$ before and after the reaction was 11.82% and 11.14%, respectively, indicating that its content remained basically stable, with only a very small amount of oxalate lost during the reaction. As presented in Figure 12b, Fe 2p corresponded to the $\text{Fe } 2p_{3/2}$ characteristic peaks of Fe(0), Fe(II) and Fe(III) at the binding energies of 707.03 eV, 710.55 eV and 712.34 eV, respectively. After the reaction, the characteristic peak of Fe(0) disappeared, and the atomic specific gravity of Fe(II) decreased, while that of Fe(III) increased, indicating that Fe(0) and Fe(II) on the surface of the material were finally oxidized to Fe(III). As shown in Figure 12c, the strength of O-H bonds was significantly weakened, and the proportion of the metal-O bonds increased due to the rusting of $n\text{Fe}^0$ from iron oxides containing Fe-O bonds and Fe-Cr-O bonds. In addition, Figure 12d indicates that the peaks with binding energies of 577.0 eV and 586 eV in the Cr 3d spectrum corresponded to low toxicity Cr(III), thus confirming the conversion of Cr(VI) to Cr(III). From these extensive findings, it can be inferred that there exists a hierarchical material consisting of an Fe^0 core, an FeC_2O_4 shell, and Fe or Fe/Cr-oxide precipitates.

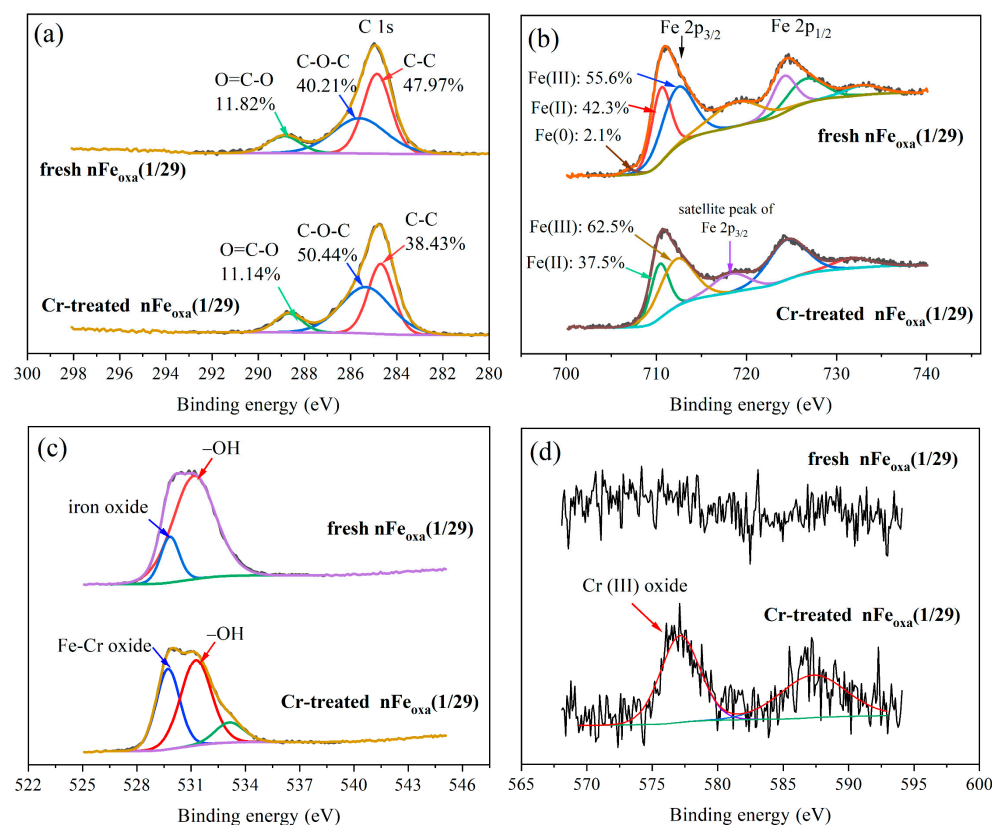


Figure 12. XPS spectra of (a) C 1s, (b) Fe 2p, (c) O 1s, and (d) Cr 2p of the fresh and Cr-treated $n\text{Fe}_{\text{oxa}}$.

As stated, the mechanisms of removal process of Cr(VI) by $n\text{Fe}_{\text{oxa}}$ mainly involved adsorption, reduction, electron transfer, and co-precipitation, as shown in Figure 13. During the preparation of $n\text{Fe}_{\text{oxa}}$, oxalate would form a complex with Fe(II), and together with the $n\text{Fe}^0$ crystal nucleus, form a composite material of ferrous oxalate and zero-valent iron. This composite structure endowed $n\text{Fe}_{\text{oxa}}$ with higher stability than $n\text{Fe}^0$, and decreased the surface iron oxide passivation layer. According to the electrochemical characterization results, more charges in $n\text{Fe}_{\text{oxa}}$ could migrate from the Fe^0 core to surface, which conformed

to the theoretical speculation regarding the formation of “d-p” conjugation between the “p” orbital of the conjugated π bond in the oxalate and the “d” orbital of the Fe atom to enhance the electron cloud density of the iron atom. This enhancement in electron density also strengthened the adsorption of CrO_4^{2-} by nFe_{oxa} . Simultaneously, the surface Fe(II) active components were more likely to receive electrons migrated from Fe^0 to be regenerated after the redox reaction with Cr(VI), instead of generating more surface free Fe(II) to achieve Cr(VI) restoration. Eventually the product of the redox reaction, Cr(III), was unstable in the aqueous solution and liable to form $\text{Cr}(\text{OH})_3$ and Fe-Cr hydroxide precipitates that would adhere and deposit on the surface of the material.

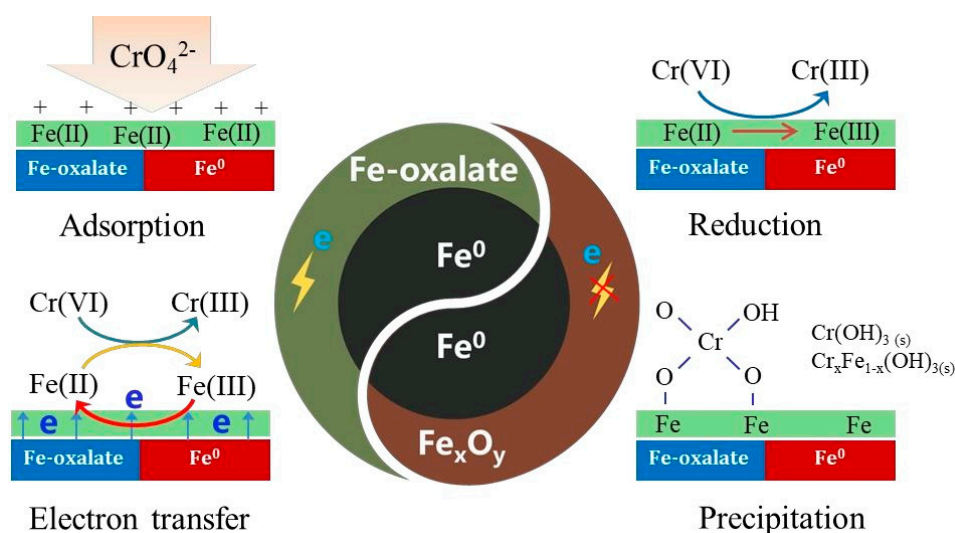


Figure 13. Mechanism for Cr(VI) removal by nFe_{oxa} .

4. Conclusions

In the present study, oxalate-modified nano zero-valent iron (nFe_{oxa}) was successfully synthesized through a liquid-phase reduction method, where oxalic acid acted as both a coordination ligand and a structural regulator to construct a $\text{FeC}_2\text{O}_4/\text{nFe}^0$ heterostructure. The composite demonstrated exceptional Cr(VI) removal efficiency (100% within 20 min at an optimal oxalate/Fe molar ratio of 1/29), outperforming conventional nFe^0 systems. Key findings include:

Electron transfer enhancement: Electrochemical analyses (EIS, LSV) revealed that oxalate ligands facilitated rapid electron transport from the Fe^0 core to the surface, dynamically regenerating Fe(II) active sites. This mechanism compensated for the reduced specific surface area (BET data) and dominated the redox process.

Selective ion effects: divalent cations (Ca^{2+} , Mg^{2+}) promoted Cr(VI) reduction via electrostatic interactions, while oxyanions (e.g., PO_4^{3-}) and humic acid competitively inhibited reactivity by blocking surface sites.

Reusability and stability: nFe_{oxa} retained >50% Cr(VI) removal efficiency after 5 cycles—a significant improvement over previous systems (33.4% decline), underscoring its environmental compatibility.

Immobilization mechanism: STEM mapping and XPS spectra confirmed that Cr(VI) was reduced to Cr(III) and immobilized through co-precipitation with Fe(II/III)–oxalate complexes, effectively mitigating secondary contamination.

This work not only provides a ligand-engineering strategy to design durable nFe^0 -based materials but also decouples the roles of electron transfer kinetics and surface area in heavy metal remediation. The insights into semiconductor-mediated redox mecha-

nisms offer a framework for optimizing nanomaterial design toward sustainable water treatment applications.

Author Contributions: Conceptualization, S.H. and J.D.; methodology, J.D.; software, C.Y.; validation, S.H., H.L. and S.Q.; formal analysis, S.H.; investigation, S.H.; resources, J.D.; data curation, S.H.; writing—original draft preparation, S.H.; writing—review and editing, J.D. and C.Y.; visualization, S.H.; supervision, J.B.; project administration, J.B.; funding acquisition, J.D. All authors have read and agreed to the published version of the manuscript.

Funding: This research was funded by the National Natural Science Foundations of China, grant No. 41907153, and the Foundations of Hubei key Laboratory of Pollution Damage Assessment and Environmental Health Risk Prevention and Control, grant No. HAES-HJJK202303.

Data Availability Statement: All raw data are available upon request from the corresponding author.

Acknowledgments: The synthesis and characterization of oxalate-modified $n\text{Fe}^0$ ($n\text{Fe}_{\text{oxa}}$) were carried out with support of the National Natural Science Foundations of China (project number 41907153) and the Foundations of Hubei key Laboratory of Pollution Damage Assessment and Environmental Health Risk Prevention and Control (project number HAES-HJJK202303).

Conflicts of Interest: The authors declare no conflicts of interest.

References

1. Gan, R.; Ye, Y.; Zhan, Z.; Zhang, Q.; Deng, Y.; Liu, Y.; Li, H.; Wan, J.; Pei, X.; Li, Q.; et al. One-step strategy for efficient Cr(VI) removal via phytate modified zero-valent iron: Accelerated electron transfer and enhanced coordination effect. *J. Hazard. Mater.* **2024**, *466*, 133636. [[CrossRef](#)]
2. Xie, X.; You, Y.; Fan, Z.; Sheng, G.; Ma, J.; Huang, Y.; Xu, H. Controllable integration of nano zero-valent iron into MOFs with different structures for the purification of hexavalent chromium-contaminated water: Combined insights of scavenging performance and potential mechanism investigations. *Sci. Total Environ.* **2024**, *935*, 173395.
3. Liao, J.; Wu, Y.; Chen, X.; Yu, H.; Lin, Y.; Huang, K.; Zhang, J.; Zheng, C. Light-triggered oxidative activity of chromate at neutral pH: A colorimetric system for accurate and on-site detection of Cr(VI) in natural water. *J. Hazard. Mater.* **2022**, *440*, 129812. [[CrossRef](#)]
4. Chen, A.; Huang, Y.; Liu, H. Fabrication of Chitin microspheres supported sulfidated nano zerovalent iron and their performance in Cr (VI) removal. *Chemosphere* **2023**, *338*, 139609. [[CrossRef](#)] [[PubMed](#)]
5. Wu, H.; Wang, R.; Ma, Y.; Zhang, T.; Yu, Y.; Lan, J.; Du, Y. Changes of MRGs and ARGs in *Acinetobacter* sp. SL-1 used for treatment of Cr(VI)-contaminated wastewater with waste molasses as carbon source. *Sci. Total Environ.* **2024**, *919*, 170770. [[CrossRef](#)]
6. Liu, X.; Chen, M.; Wang, D.; Du, F.; Xu, N.; Sun, W.; Han, Z. Cr(VI) removal during cotransport of nano-iron-particles combined with iron sulfides in groundwater: Effects of *D. vulgaris* and *S. putrefaciens*. *J. Hazard. Mater.* **2024**, *472*, 134583. [[CrossRef](#)]
7. Mu, Y.; Jia, F.; Ai, Z.; Zhang, L. Iron oxide shell mediated environmental remediation properties of nano zero-valent iron. *Environ. Sci.-Nano* **2017**, *4*, 27–45. [[CrossRef](#)]
8. Wang, Y.; Xu, J.; Yang, K.; Lin, D. A versatile nanocomposite $\text{Fe}^0/\text{SiO}_2/\text{CaO}_2$ for reductive, oxidative, and coagulation removal of organic and inorganic contaminants from water. *Biochem. Eng. J.* **2023**, *454*, 140048. [[CrossRef](#)]
9. Zou, Y.; Wang, X.; Khan, A.; Wang, P.; Liu, Y.; Alsaedi, A.; Hayat, T.; Wang, X. Environmental remediation and application of nanoscale zero valent iron and its composites for the removal of heavy metal ions: A review. *Environ. Sci. Technol.* **2016**, *50*, 7290–7304. [[CrossRef](#)]
10. Ling, L.; Huang, X.; Li, M.; Zhang, W. Mapping the reactions in a single zero-valent iron nanoparticle. *Environ. Sci. Technol.* **2017**, *51*, 14293–14300. [[CrossRef](#)]
11. Wang, X.; Yuan, S.; Kong, J.; Chen, C.; Yu, C.; Huang, L.; Sun, H.; Peng, X.; Hu, Y. Tea saponin co-ball milled commercial micro zero-valent iron for boosting Cr(VI) removal. *J. Hazard. Mater.* **2024**, *473*, 134668. [[CrossRef](#)] [[PubMed](#)]
12. Sohn, K.; Kang, S.-K.; Ahn, S.; Woo, M.; Yang, S. $\text{Fe}(0)$ nanoparticles for nitrate reduction: Stability, reactivity, and transformation. *Environ. Sci. Technol.* **2006**, *40*, 5514–5519. [[CrossRef](#)] [[PubMed](#)]
13. Zhu, N.; Li, Y.; Zhang, F. Catalytic dechlorination of polychlorinated biphenyls in subcritical water by Ni/Fe nanoparticles. *Chem. Eng. J.* **2011**, *171*, 919–925. [[CrossRef](#)]

14. Huang, D.; Hu, Z.; Peng, Z.; Zeng, G.; Chen, G.; Zhang, C.; Cheng, M.; Wan, J.; Wang, X.; Qin, X. Cadmium immobilization in river sediment using stabilized nanoscale zero-valent iron with enhanced transport by polysaccharide coating. *J. Environ. Manag.* **2018**, *210*, 191–200. [\[CrossRef\]](#)
15. Zhou, L.; Li, Z.; Yi, Y.; Tsang, E.; Fang, Z. Increasing the electron selectivity of nanoscale zero-valent iron in environmental remediation: A review. *J. Hazard. Mater.* **2022**, *421*, 126709. [\[CrossRef\]](#)
16. Wang, M.; Chen, Y.; Zhang, Y.; Zhao, K.; Feng, X. Selective removal of Cr(VI) by tannic acid and polyethyleneimine modified zero-valent iron particles with air stability. *J. Hazard. Mater.* **2023**, *458*, 132018. [\[CrossRef\]](#)
17. Hang, X.; Wang, W.; Ling, L.; Zhang, W. Heavy metal-nZVI reactions: The core-shell structure and applications for heavy metal treatment. *Acta Chim. Sin.* **2017**, *75*, 529–537. [\[CrossRef\]](#)
18. Zhu, N.; Xu, Y.; Dai, L.; Zhang, Y.; Hu, G. Application of sequential extraction analysis to Pb(II) recovery by zerovalent iron-based particles. *J. Hazard. Mater.* **2018**, *351*, 138–146. [\[CrossRef\]](#)
19. Gu, Y.; Wang, B.; He, F.; Bradley, M.; Tratnyet, P. Mechanochemically Sulfidated Microscale Zero Valent Iron: Pathways, Kinetics, Mechanism, and Efficiency of Trichloroethylene Dechlorination. *Environ. Sci. Technol.* **2017**, *51*, 12653–12662. [\[CrossRef\]](#)
20. Li, J.; Zhang, X.; Sun, Y.; Liang, L.; Pan, B.; Zhang, W.; Guan, X. Advances in sulfidation of zerovalent iron for Water decontamination. *Environ. Sci. Technol.* **2017**, *51*, 13533–13544. [\[CrossRef\]](#)
21. Lin, X.; He, X.; Lei, L.; Zhao, Y.; Cui, L.; Wu, G. Development of ionic liquid filled chitosan capsules to remove Cr(VI) from acidic solution: Adsorption properties and mechanism. *J. Environ. Chem. Eng.* **2022**, *10*, 108081. [\[CrossRef\]](#)
22. Li, H.; Wang, J.; Wang, R.; Huang, K.; Luo, W.; Tao, X.; Dang, Z.; Yin, H.; Guo, C.; Lu, G. Debromination of 2,2',4,4'-tetrabromodiphenyl ether (BDE-47) by synthetic Pd/Fe⁰ and Cu/Fe⁰ in different protic solvents. *Chemosphere* **2018**, *212*, 946–953. [\[CrossRef\]](#) [\[PubMed\]](#)
23. Zheng, K.; Song, Y.; Wang, X.; Li, X.; Mao, X.; Wang, D. Understanding the electrode reaction process of dechlorination of 2,4-dichlorophenol over Ni/Fe nanoparticles: Effect of pH and 2,4-dichlorophenol concentration. *J. Environ. Sci.* **2019**, *84*, 13–20. [\[CrossRef\]](#)
24. Chen, L.; Ni, R.; Yuan, T.; Gao, Y.; Kong, W.; Zhang, P.; Yue, Q.; Gao, B. Effects of green synthesis, magnetization, and regeneration on ciprofloxacin removal by bimetallic nZVI/Cu composites and insights of degradation mechanism. *J. Hazard. Mater.* **2020**, *382*, 121008. [\[CrossRef\]](#)
25. Xue, W.; Huang, D.; Zeng, G.; Wan, J.; Zhang, C.; Xu, R.; Cheng, M.; Deng, R. Nanoscale zero-valent iron coated with rhamnolipid as an effective stabilizer for immobilization of Cd and Pb in river sediments. *J. Hazard. Mater.* **2018**, *341*, 381–389. [\[CrossRef\]](#)
26. Latif, A.; Sheng, D.; Sun, K.; Si, Y.; Azeem, M.; Abbas, A.; Bilal, M. Remediation of heavy metals polluted environment using Fe-based nanoparticles: Mechanisms, influencing factors, and environmental implications. *Environ. Pollut.* **2020**, *264*, 114728. [\[CrossRef\]](#)
27. Liu, J.; Liu, A.; Zhang, W. The influence of polyelectrolyte modification on nanoscale zero-valent iron (nZVI): Aggregation, sedimentation, and reactivity with Ni(II) in water. *Chem. Eng. J.* **2016**, *303*, 268–274. [\[CrossRef\]](#)
28. Kumar, M.; Bae, S.; Han, S.; Chang, Y.; Lee, W. Reductive dechlorination of trichloroethylene by polyvinylpyrrolidone stabilized nanoscale zerovalent iron particles with Ni. *J. Hazard. Mater.* **2017**, *340*, 399–406. [\[CrossRef\]](#)
29. Li, J.; Zhang, X.; Liu, M.; Pan, B.; Zhang, W.; Shi, Z.; Guan, X. Enhanced reactivity and electron selectivity of sulfidated zerovalent iron toward chromate under aerobic conditions. *Environ. Sci. Technol.* **2018**, *52*, 2988. [\[CrossRef\]](#)
30. Klimkova, S.; Cernik, M.; Lacinova, L.; Filip, J.; Jancik, D.; Zboril, R. Zero-valent iron nanoparticles in treatment of acid mine water from in situ uranium leaching. *Chemosphere* **2011**, *82*, 1178–1184. [\[CrossRef\]](#)
31. Jiang, J.-J.; Chan, A.; Ali, S.; Saha, A.; Haushalter, K.J.; Lam Macrina, W.; Parker, J.; Brenner, M.; Mahon, S.; Patel, H.; et al. Hydrogen Sulfide Mechanisms of Toxicity and Development of an Antidote. *Sci. Rep.* **2016**, *6*, 20831. [\[CrossRef\]](#) [\[PubMed\]](#)
32. Xu, J.; Avellan, A.; Li, H.; Clark, E.; Henkelman, G.; Kaegi, R.; Lowry, G. Iron and sulfur precursors affect crystalline structure, speciation, and reactivity of sulfidized nanoscale zerovalent Iron. *Environ. Sci. Technol.* **2020**, *54*, 13294–13303. [\[CrossRef\]](#)
33. Cheng, D.; Ding, H.; Tan, Y.; Yang, D.; Pan, Y.; Liao, W.; He, F. Dramatically Enhanced Phenol Degradation upon FeS Oxygenation by Low-molecular-weight Organic Acids. *J. Hazard. Mater.* **2023**, *459*, 132260. [\[CrossRef\]](#) [\[PubMed\]](#)
34. Li, W.; Feng, Q.; Li, Z.; Jin, T.; Zhang, Y.; Southam, G. Inhibition of iron oxidation in *Acidithiobacillus ferrooxidans* by low-molecular-weight organic acids: Evaluation of performance and elucidation of mechanisms. *Sci. Total Environ.* **2024**, *927*, 171919. [\[CrossRef\]](#)
35. Dakora, F.; Phillips, D. Root exudates as mediators of mineral acquisition in low-nutrient environments. *Plant Soil* **2002**, *245*, 35–47. [\[CrossRef\]](#)
36. Yang, W.; Wang, G. Activation of polycyclic aromatic hydrocarbons in soil by low molecular weight organic acids. *Mod. Gard.* **2018**, *6*, 39–41.
37. Kantar, C. Heterogeneous processes affecting metal ion transport in the presence of organic ligands: Reactive transport modeling. *Earth-Sci. Rev.* **2007**, *81*, 175–198. [\[CrossRef\]](#)

38. Vilardi, G.; Parisi, M.; Verdone, N. Simultaneous aggregation and oxidation of nZVI in Rushton equipped agitated vessel: Experimental and modelling. *Powder Technol.* **2019**, *353*, 238–246. [\[CrossRef\]](#)
39. Yuan, Y.; Wei, X.; Yin, H.; Zhu, M.; Luo, H.; Dang, Z. Synergistic removal of Cr(VI) by S-nZVI and organic acids: The enhanced electron selectivity and pH-dependent promotion mechanisms. *J. Hazard. Mater.* **2022**, *423*, 127240. [\[CrossRef\]](#)
40. Liu, X.; Dong, H.; Zeng, Q.; Yang, X.; Zhang, D. Synergistic effects of reduced nontronite and organic ligands on Cr(VI) reduction. *Environ. Sci. Technol.* **2019**, *53*, 13732–13741. [\[CrossRef\]](#)
41. Zhou, H.; He, Y.; Lan, Y.; Mao, J.; Chen, S. Influence of complex reagents on removal of chromium(VI) by zero-valent iron. *Chemosphere* **2008**, *72*, 870–874. [\[CrossRef\]](#) [\[PubMed\]](#)
42. Hug, S.-J.; Laubscher, H.; James, B. Iron(III) Catalyzed Photochemical Reduction of Chromium(VI) by Oxalate and Citrate in Aqueous Solutions. *Environ. Sci. Technol.* **1997**, *31*, 160–170. [\[CrossRef\]](#)
43. Gadol Hayley, J.; Flynn Elaine, D.; Catalano Jeffrey, G. Oxalate-Promoted Trace Metal Release from Crystalline Iron Oxides under Aerobic Conditions. *Environ. Sci. Technol. Lett.* **2017**, *4*, 311–315. [\[CrossRef\]](#)
44. Xie, L.; Chen, Q.; Liu, Y.; Ma, Q.; Zhang, J.; Tang, C.; Duan, G.; Lin, A.; Zhang, T.; Li, S. Enhanced remediation of Cr(VI)-contaminated soil by modified zero-valent iron with oxalic acid on biochar. *Sci. Total Environ.* **2023**, *905*, 167399. [\[CrossRef\]](#)
45. Wu, S.; Han, X.; Xia, F.; Yang, Y.; Xu, X.; Deng, S.; Jiang, Y. Enhanced Degradation of 2,4-DNT in Groundwater by Oxalic Acid-Modified Zero-Valent Iron as Persulfate Activator. *Res. Environ. Sci.* **2022**, *35*, 108–118.
46. Li, M.; Dai, H.; Zhan, P.; Tan, C.; Ning, Z.; Hu, F.; Xu, X.; Peng, X. Rapid reduction of aqueous Cr(VI) by oxalic acid on N-doped lignin charcoal: A significant contribution of structural defects and electronic shuttle effect. *J. Clean. Prod.* **2023**, *415*, 137883. [\[CrossRef\]](#)
47. Su, Y.; Adeleye, A.; Keller, A.; Huang, Y.; Dai, C.; Zhou, X.; Zhang, Y. Magnetic sulfide-modified nanoscale zerovalent iron (S-nZVI) for dissolved metal ion removal. *Water Res.* **2015**, *74*, 47–57. [\[CrossRef\]](#)
48. Liao, M.; Wang, X.; Cao, S.; Li, M.; Peng, X.; Zhang, L. Oxalate Modification Dramatically Promoted Cr(VI) Removal with Zero-Valent Iron. *ACS ES&T Water* **2021**, *1*, 2109–2118.
49. Flynn, E.; Catalano, J. Competitive and Cooperative Effects during Nickel Adsorption to Iron Oxides in the Presence of Oxalate. *Environ. Sci. Technol.* **2017**, *51*, 9792–9799. [\[CrossRef\]](#)
50. Situm, A.; Rahman, M.; Goldberg, S. Spectral characterization and surface complexation modeling of low molecular weight organics on hematite nanoparticles: Role of electrolytes in the binding mechanism. *Environ. Sci. Nano* **2016**, *3*, 910–926. [\[CrossRef\]](#)
51. Huang, M.; Zhou, T.; Wu, X.; Mao, J. Distinguishing homogeneous-heterogeneous degradation of norfloxacin in a photochemical Fenton-like system (Fe_3O_4 /UV/oxalate) and the interfacial reaction mechanism. *Water Res.* **2017**, *119*, 47–56. [\[CrossRef\]](#) [\[PubMed\]](#)
52. Kar, A.; Acharya, A.; Mundlapati, V.; Pradhan, G.; Biswal, H.; Dash, A. Ligand substitution and electron transfer reactions of trans-(diaqua)(salen)manganese(III) with oxalate: An experimental and computational study. *RSC Adv.* **2014**, *4*, 58867–58879. [\[CrossRef\]](#)
53. Jiang, W.; Cai, Q.; Xu, W.; Yang, M.; Cai, Y.; Dionysiou, D.; O'Shea, K. Cr(VI) Adsorption and Reduction by Humic Acid Coated on Magnetite. *Environ. Sci. Technol.* **2014**, *48*, 8078–8085. [\[CrossRef\]](#) [\[PubMed\]](#)
54. Liu, J.; Zhao, Z.; Jiang, G. Efficient Removal of Cr(VI) from Aqueous Solution with $\text{Fe@Fe}_2\text{O}_3$ Core–Shell Nanowires. *Environ. Sci. Technol.* **2008**, *42*, 6955–6960.
55. Tang, C.; Huang, Y.; Zeng, H.; Zhang, Z. Reductive removal of selenate by zero-valent iron: The roles of aqueous Fe^{2+} and corrosion products, and selenate removal mechanisms. *Water Res.* **2014**, *67*, 166–174. [\[CrossRef\]](#)
56. Tang, C.; Huang, Y.; Zeng, H.; Zhang, Z. Promotion effect of Mn^{2+} and Co^{2+} on selenate reduction by zero-valent iron. *Chem. Eng. J.* **2014**, *244*, 97–104. [\[CrossRef\]](#)
57. Bae, S.; Hana, K. Reactivity of Nanoscale Zero-Valent Iron in Unbuffered Systems: Effect of pH and Fe(II) Dissolution. *Environ. Sci. Technol.* **2015**, *49*, 10536–10543. [\[CrossRef\]](#)
58. Lim, T.; Zhu, B. Effects of anions on the kinetics and reactivity of nanoscale Pd/Fe in trichlorobenzene dechlorination. *Chemosphere* **2008**, *73*, 1471–1477. [\[CrossRef\]](#)
59. Kim, J.; Shea, P.; Yang, J.; Kim, J. Halide salts accelerate degradation of high explosives by zerovalent iron. *Environ. Pollut.* **2007**, *147*, 634–641. [\[CrossRef\]](#)
60. Yin, W.; Wu, J.; Li, P.; Wang, X.; Zhu, N.; Wu, P.; Yang, B. Experimental study of zero-valent iron induced nitrobenzene reduction in groundwater: The effects of pH, iron dosage, oxygen and common dissolved anions. *Chem. Eng. J.* **2012**, *184*, 198–204. [\[CrossRef\]](#)
61. Yan, S.; Hua, B.; Bao, Z.; Yang, J.; Liu, C.; Deng, B. Uranium(VI) Removal by Nanoscale Zerovalent Iron in Anoxic Batch Systems. *Environ. Sci. Technol.* **2010**, *44*, 7783–7789. [\[CrossRef\]](#) [\[PubMed\]](#)
62. Hou, S.; Tian, H.; Huang, C.; Wang, P.; Zeng, Q.; Peng, H.; Liu, S.; Li, A. Removal of Cr(VI) from aqueous solution by amino-modified biochar supported nano zero-valent iron. *Acta Sci. Circumstantiae* **2020**, *40*, 3931–3938.
63. Lv, X.; Hu, Y.; Tang, J.; Sheng, T.; Jiang, G.; Xu, X. Effects of co-existing ions and natural organic matter on removal of chromium (VI) from aqueous solution by nanoscale zero-valent iron (nZVI)- Fe_3O_4 nanocomposites. *Chem. Eng. J.* **2013**, *218*, 55–64. [\[CrossRef\]](#)

64. Mak, M.; Rao, P.; Lo, I. Effects of hardness and alkalinity on the removal of arsenic(V) from humic acid-deficient and humic acid-rich groundwater by zero-valent iron. *Water Res.* **2009**, *43*, 4296–4304. [[CrossRef](#)]
65. Tanboonchuy, V.; Grisdanurak, N.; Liao, C. Background species effect on aqueous arsenic removal by nano zero-valent iron using fractional factorial design. *J. Hazard. Mater.* **2012**, *205–206*, 40–46. [[CrossRef](#)]
66. Liu, H.; Chen, T.; Chang, D.; Chen, D.; Liu, Y.; He, H.; Yuan, P.; Frost, R. Nitrate reduction over nanoscale zero-valent iron prepared by hydrogen reduction of goethite. *Mater. Chem. Phys.* **2012**, *133*, 205–211. [[CrossRef](#)]
67. Ryu, A.; Jeong, S.; Jang, A.; Choi, H. Reduction of highly concentrated nitrate using nanoscale zero-valent iron: Effects of aggregation and catalyst on reactivity. *Appl. Catal. B Environ.* **2011**, *105*, 128–135. [[CrossRef](#)]
68. Zhang, J.; Hao, Z.; Zhen, Z.; Yang, Y.; Xu, X. Kinetics of nitrate reductive denitrification by nanoscale zero-valent iron. *Process Saf. Environ. Prot.* **2010**, *88*, 439–445. [[CrossRef](#)]
69. Wang, Q.; Cissoko, N.; Zhu, M.; Xu, X. Effects and mechanism of humic acid on chromium(VI) removal by zero-valent iron (Fe⁰) nanoparticles. *Phys. Chem. Earth Parts A/B/C* **2011**, *36*, 442–446. [[CrossRef](#)]
70. Zhu, X.; Thao, T.; Du, J.; Xu, T.; Cui, Y.; Ling, H.; Kim, S. Novel core-shell sulfidated nano-Fe(0) particles for chromate sequestration: Promoted electron transfer and Fe(II) production. *Chemosphere* **2021**, *284*, 131379. [[CrossRef](#)]

Disclaimer/Publisher’s Note: The statements, opinions and data contained in all publications are solely those of the individual author(s) and contributor(s) and not of MDPI and/or the editor(s). MDPI and/or the editor(s) disclaim responsibility for any injury to people or property resulting from any ideas, methods, instructions or products referred to in the content.